SIMULATION OF FLOW PAST A CYLINDER WITH ADAPTIVE SPECTRAL ELEMENT METHOD

L.-C. Hsu* J.-Z. Ye C.-H. Hsu

Department of Mechanical Engineering
National Yunlin University of Science and Technology
Yunlin, Taiwan

ABSTRACT

The simulations of flow past a two-dimensional circular cylinder are conducted to investigate the feasibility of adaptive mesh refinement applied on curved spectral elements. The nonconforming spectral element method and adaptive meshes technique are used to the curve surfaces and observe whether any discontinuity of the solutions. The adaptive nonconforming spectral element method is implemented to compare with those obtained by conforming mesh method with respect to several existing numerical and experimental studies. Meanwhile, three kinds of estimated error base mesh adaptation are conducted to compare their accuracy and efficiency with conforming mesh method. The results show adaptive nonconforming mesh method is more efficient than the conforming method. Especially, the vorticity error based method performs highest accuracy and fastest convergence. The results show this mesh refinement technique is applicable on the curved elements with satisfactory accuracy. It releases this technique may be applied on the simulations of flow past objects with more general geometries.

Keywords: Adaptive meshes, Vorticity based, Spectral element, Cylinder, Vortex.

1. INTRODUCTION

Although spectral element method preserves the nature of high accuracy and fast convergence [1], it is still expensive to solve practical problems. Maday *et al*. [2, 3] broke the limit by developing the mortar element methods for nonconforming spectral elements. Mavriplis and Hsu [4] developed an adaptive spectral element method based on 2D mortar element method to solve Navier-Stokes equations for incompressible flow and later the method was applied on the simulations of thin flame front phenomena [5]. Further, the method was extended to the 3D mortar element method for solving Poisson problem by Feng *et al*. [6]. Henderson [7] developed another nonconforming element method, namely, the piecewise mortar element method by incorporating dynamic meshes for 2D incompressible flow simulation. Further, the nonconforming element method has also been extended to be three-dimensional scheme with the Fourier expansion technique for turbulence flow simulation.

Premasuthan *et al.* [8] applied the spectral difference method and the mortar element method with mesh refinement on high-order computation for compressible fluid flows with discontinuities such as supersonic flow past a bump, transonic flow past an airfoil and supersonic flow past a cylinder. A tree-based adaptive mesh refinement (AMR) algorithm for the high-order discontinuous Galerkin method on quadrilateral grids with nonconforming elements is proposed by Kopera and Giraldo [9] to solve the atmospheric simulations which require highly expensive large computational cost. In that study, the solution for dealing with nonconforming faces fluxes is based on mortar element method. The rising thermal bubble case and the general features of the solution are tested and captured correctly by AMR simulations with 15 times speed-up.

Dupond and Lin [10] used the adaptive triangular spectral element method to simulate a shallow water problem and compare the results with finite difference methods as well as the finite element method. The results show the spectral element method is superior to finite element methods in energy conservation with no dissipation and higher accuracy within the same CPU time. Although the adaptive spectral element method is better than the spectral element and finite difference methods [10], however, the accuracy-to-cost convergence is not as good as that achieved by the spectral element method.

In this study, for investigation of the performance of the adaptive spectral element method and the verification of the accuracy of mesh refinement on curved elements, simulations of flow past a circular cylinder in Re = 100,140 and Re = 200, respectively, are implemented to compare the results obtained by conforming spectral element method respect to several existing numerical and experimental studies.

* Corresponding author (edhsu@yuntech.edu.tw)

DOI : 10.1017/jmech.2016.77
Copyright © 2016 The Society of Theoretical and Applied Mechanics
https://doi.org/10.1017/jmech.2016.77 Published online by Cambridge University Press

2. NUMERICAL METHOD

The incompressible Navier-Stokes equations are solved to simulate the flows in the laminar regime as the following manners.

$$\frac{\partial \vec{u}}{\partial t} + \vec{u} \cdot \nabla \vec{u} = -\frac{1}{\rho} \nabla p + \nu \nabla^2 \vec{u} \tag{1}$$

$$\nabla \cdot \vec{u} = 0 \tag{2}$$

where $\vec{u}$ is the velocity vector; p is the pressure; ρ is the density and ν is the kinematic viscosity. For the computational efficiency, a time splitting scheme [11] is introduced to separate the nonlinear convective terms from the diffusion terms. The nonlinear convective term is treated explicitly by using a third order Adam-Bashforth scheme with coefficients, β_r, due to its low dispersion errors and relatively large part of the imaginary axis included within the absolute stability region [12]. The diffusion and pressure terms are treated and governed by Helmholtz models as follows.

$$(\nabla^2 - \lambda^2)u = g \tag{3}$$

The variational form of Eq. (3) with an arbitrary trial function $\varphi = \delta u$

$$-\int_\Omega \nabla u \cdot \nabla \psi \, dx - \lambda^2 \int_\Omega u\psi \, dx = \int_\Omega g\psi \, dx \qquad \forall \psi \tag{4}$$

The integral in Eq. (4) can be approximated by Gauss-Lobatto quadrature. All variables can be approximated by discretization as follows,

$$u_h^k = \sum_{p=0}^{N} \sum_{q=0}^{M} u_{pq}^k h_p(r) h_q(s) \tag{5}$$

where, the h functions are the Lagrangian interpolants as shown in Eq. (6) based on the orthogonal set of Legendre polynomials, L_N, of degree of order N (or M) and r, s are the local coordinates on each element k.

$$h_i(r) = -\frac{1}{N(N+1)L_N(\xi_i)} \frac{(1-r^2)L_N'(r)}{r-\xi_i} \tag{6}$$

By performing Gauss-Lobatto quadrature in integral, Lagrangian interpolation and summing contributions from adjacent elements, the global matrix equation is obtained as follows,

$$\sum_k^K \left(A_{\alpha\beta pq}^k - \lambda^2 B_{\alpha\beta pq}^k \right) u_{pq}^k = \sum_k^K B_{\alpha\beta pq}^k g_{pq}^k \tag{7}$$

where $A_{\alpha\beta pq}^k$ is the stiffness matrix and $B_{\alpha\beta pq}^k$ is the mass matrix, K is total element number. The expression is simplified to be

$$(A - \lambda^2 B)u = Bg \tag{8}$$

where A is the discrete Laplacian operator and B the mass matrix. This discretized form represents a set of two-dimensional Helmholtz equation for solving diffusion and pressure terms in Navier-Stokes equations. Here, the matrix equation is solved by preconditioned conjugate gradient [13].

2.1 Nonconforming Approach

The nonconforming spectral element method only requires minimum L^2 error on the interfaces between elements rather than C^0 continuity which is required by the conforming spectral element method. The advantages of this method are that it preserves the exponential convergence property of spectral element discretization and decouples the locally structured internal element in each subdomain and elemental interface data evaluation while naturally imposing the continuity condition in intensive subdomain calculation with a minimum of communication between elements.

On the interface between elements, there is mortar function which is charged to sum every elemental contribution on common elemental boundaries. With a set of transform matrices called projection operators, the solutions of local elements are projected to the common boundaries where mortar functions are weighted by the dimensions of the elements on the common boundary to sum all elemental contributions. The transpose matrices of projection operators also serve to project solutions from common boundary to the local boundaries of the elements as described schematically in Fig. 1.

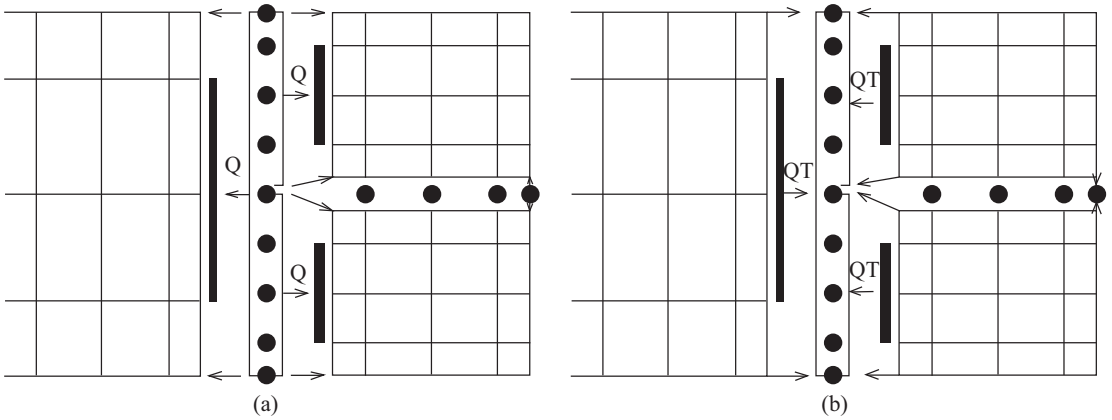


Fig. 1 Communication of nonconforming mesh: (a) projection operator from mortars to local edges, (b) projection operator from local edges to mortars. ●: mortar points, Q: projection matrix from mortar to local edge, Q^T: transpose projection matrix from local edge to mortar.

https://doi.org/10.1017/jmech.2016.77 Published online by Cambridge University Press

The elemental boundary, $\partial\Omega$, composed of four edges, Γ. The mortar, γ^p, is defined as the interface of arbitrary two adjacent elements. The mortar space, S, is the union of all mortars. The auxiliary mortar space is defined as the Eq. (9),

$$W_h = \{\phi \in C^0(S), \forall p = 1,\ldots,M, \phi|_{\gamma^p} \in P_N(\gamma^p)\ \ \phi|_{\partial\Omega} = 0\} \tag{9}$$

where $P_N(\gamma^p)$ is the space of all polynomials on γ^p of degree $\leq$ N. $\phi|_{\gamma^p}$ is mortar function. The nonconforming space for solutions on the elemental edges is given as

$X_h = \{u \in L^2(\Omega), \forall k = 1,\ldots,K\ u|_{\Omega^k} \in P_N(\Omega^\kappa)$ such that $\exists \phi \in W_h$ for which:

$\forall q = 1,\ldots,V \quad \forall k = 1,\ldots,K,$ such that u^q is a vertex of Ω^k,

$$u|_{\Omega^\kappa}(u^q) = \phi(u^q) \tag{10}$$

and

$$\begin{aligned} &\forall l = 1,\ldots,4 \quad \forall k = 1,\ldots,K \\ &\forall \psi \in P_{N-2}(\Gamma^{k,l}) \quad \int_{\Gamma^{k,l}} (u|_{\Omega^k} - \phi)\psi\, ds = 0\} \end{aligned} \tag{11}$$

where M is total number of mortar elements; V is the total number of vertices; K is the total number of elements. To avoid losing accuracy in nonconforming meshes, on the common boundaries, the L^2 condition, Eq. (11), is applied to minimize the jump between the solution on elemental edge and its corresponding mortar function. Further, the vertex pinning condition, Eq. (10), is applied to preserve exact continuity at cross points. The L^2 and vertex conditions can be represented in discrete forms by choosing the basis function, ψ, as follows.

$$\psi|_{\Gamma^{k,l}} = \sum_{q=0}^{N-1} \beta_q \eta_q^{N-2}(\hat{s}) \tag{12}$$

where,

$$\eta_q^{N-2}(z) = (-1)^{N-q} \frac{L_N'(z)}{\varepsilon_q - z} \quad z \in |-1,1| \quad q \in \{1,\ldots,N-1\} \tag{13}$$

The mortar function, $\phi|_{\gamma^p}$, exists on the edges of an element. Therefore it can be expressed by one-dimensional interpolants as

$$\phi|_{\gamma^p} = \sum_{j=0}^{N} \phi_j^p h_j^N(\tilde{s}) \quad \forall p \in \{1,\ldots,M\} \tag{14}$$

where the h_j^N are Lagrangian interpolants and $\tilde{s}$ is the local mortar coordinate.

The discrete mortar function, local elemental boundary solution and basis are applied in the L^2 condition, as in Eq. (11).

$$\int_\Gamma u\psi \cdot ds = \int_\Gamma \phi\psi \cdot ds \tag{15}$$

The integrals in Eq. (15) are performed by the Gauss-Lobatto Legendre quadrature as follows.

$$\sum_{j=1}^{N-1} B_{i,j} u_j = \sum_{j=0}^{N} P_{i,j} \phi_j \tag{16}$$

The Eq. (16) can be simply represented by matrix form and multiplied by inverse matrix, B^{-1}, on both sides of equation. The product of $B^{-1}P$ can be represented by a matrix Q. Eq. (16) can be simplified to be Eq. (17).

$$\vec{u}_b = Q\vec{\phi} \tag{17}$$

where ϕ is the solution in mortar space; u_b is the solution in elemental boundary which can be obtained by mortar solution, ϕ, multiplied by matrix Q. Hence, Q is so called projection matrix which deals with the solution projection from mortar spaces to elemental boundaries. Q^T is the matrix for residual projection from elemental boundaries to mortar spaces.

$$\vec{u} = \begin{bmatrix} u_i \\ u_b \end{bmatrix} = \begin{bmatrix} I & 0 \\ 0 & Q \end{bmatrix} \begin{bmatrix} \vec{u}_i \\ \vec{\phi} \end{bmatrix} = \tilde{Q}\tilde{u} \tag{18}$$

where u_i is internal unknowns in a element; $\tilde{u}$ represents all unknowns which include mortar points and internal unknowns. The global form of projection matrices are $\hat{Q}$ and $\hat{Q}^T$, respectively [14]. The nonconforming discrete form of Helmholtz equation is shown in Eq. (19) which is the counter part of conforming form, Eqn. (8).

$$\hat{Q}^T(A - \lambda^2 B)\hat{Q}u = \hat{Q}^T Bg \tag{19}$$

where, A is the discrete global Laplacian operator matrix. B is the global mass matrix and u is the local solutions in elements. Furthermore, Eq. (19) can be solved by conjugate gradient due to the property of the symmetric positive definite matrix.

3. VORTICITY BASED MESH REFINEMENT

For mesh adapdation, several physical properties can be used as the indicators For example, the discontinuity of density and velocity are most commonly used in compressible flow. The derivatives of velocity or pressure are usually used in smooth solutions such as for incompressible flow. Oh *et al*. [15] used the finite diference method to simulate vortex shedding behind a circular cylinder by applying adaptive meshes with the error indicator which was composed of the truncation error of the magnitude of the density gradient and density change of the time rate. Rausch *et al*. [16] proposed using the absolute value of the substantial derivative of density as an enrichment indicator. Hwang and Kuo [17] introduced a new mesh-enrichment indicator which is based on the gradient of the substantial derivative of density.

https://doi.org/10.1017/jmech.2016.77 Published online by Cambridge University Press

A time dependent adaptive nonconforming approach combines the nonconforming spectral element method and adaptive mesh refinement scheme [4]. Though, this mesh refinement method based on the estimated error decay rate, σ, performs well in steady cases, it is not reliable for solving unsteady or transient problems such as flow past an inclined flat plate or cylinder. Furthermore, mesh refinement guided by other physical properties such as velocity and pressure may improve the solution but without guarantee. Hence, to solve the problems in the simulation of unsteady cases, the vorticity based mesh refinement is proposed. The present mesh refinement scheme is based on the estimated error of vorticity which is related to first derivative of velocities as Eq. (20). This approach by minimizing the error from the gradient of properties rather than the original physical properties may avoid the error propagation and obtain higher accuracy.

$$\omega = \left(\frac{\partial v}{\partial x} - \frac{\partial u}{\partial y} \right) \tag{20}$$

3.1 Indicators of Mesh Adaptation

During every period of computation, the estimated error is used as the indicator of mesh adaptation. The exact solution can be expressed by sum of infinite terms of Legendre polynomials. However, the numerical approach truncates solution to be sum of finite terms and results in truncation error. Besides, once the numerical solution deviates from the best polynomial fit, it exerts the quadrature error. Therefore, the elemental estimated error is the sum of the truncation error and quadrature error as shown in the following equation.

$$\varepsilon_{est}^{k} = \left(\frac{(a_N^k)^2}{\frac{2N+1}{2}} + \int_{N+1}^{\infty} \frac{(a_n^k(n))^2}{\frac{2n+1}{2}} \right)^{\frac{1}{2}} \tag{21}$$

The Legendre polynomial coefficients, $a_{n,}$ can be obtained by solved solution and orthogonal relationship between polynomials. However, the solved solutions are not available beyond the finite term, N, to compute the polynomial coefficients for truncated part. Hence, the coefficient, a_n, is assumed to decay exponentially shown in Eq. (22) as the polynomial order, N, is increased, when n > N.

$$a_n = Ce^{-\sigma n} \tag{22}$$

In each dimension, the coefficients of the last four known points, $a_{n,}$ n = N-3, N, were used with the least squares best fit method to extrapolate the coefficient, C, and the decay rate, σ. The decay rate, σ, can be use to represent the quality of resolution. Generally, the result is regarded as having poor resolution when σ < 1 and good resolution when σ > 1.

Because the areas around the vortex centers is predicted to hold stronger vorticity gradient, the estimated errors of vorticity are used as the indicator of mesh refinement to capture more accurate vorticity. Hence, to describe vortex shedding phenomena precisely, obtaining more accurate vorticity is crucial. The estimated errors of vorticity can be obtained according to the following procedure.

1) Obtain vorticity, ω_h, by solving Navier-Stokes equations.
2) Compute the coefficients of Legendre of polynomials, a_N, by utilizing the orthogonal property as the following. The integral can be solved by Gauss-Lobatto Legendre quadrature.

$$a_n = \frac{2n+1}{2} \int_{-1}^{1} \omega_h(x(r)) L_n(r) dr \tag{23}$$

3) Use last four terms of coefficients, a_n, n = N to N-3 to extrapolate the decay rate of coefficient for n = N + 1, ∞.
4) Input required a_N and decay rate, σ, to Eq. (21), the estimated errors of vorticity are obtained.

Meanwhile, three kinds of properties are selected as mesh refinement indicators to compare their accuracy and efficiency of computation, including estimated error of synthesis of velocity and pressure, estimated error of vorticity and decay rate (σ) of estimated error. The estimated error by synthesis of velocity and pressure selects larger error from the field of velocity or pressure as representative error. If the estimated error coefficient decay rate σ is used as the indicator, only the elements with σ < 0.8 are selected for mesh refinement. During performing each kind of error estimation, the element with largest estimated error is chosen to be refined. The meshes are refined and the existing data is used to interpolate on the new grids for the next time step of computation.

4. RESULTS AND DISCUSSION

4.1 Boundary Conditions

A rectangular global computational domain is selected as Fig. 2. The diameter of cylinder (D) is 1 unit. The domain is extended a distance of 20D in upstream from

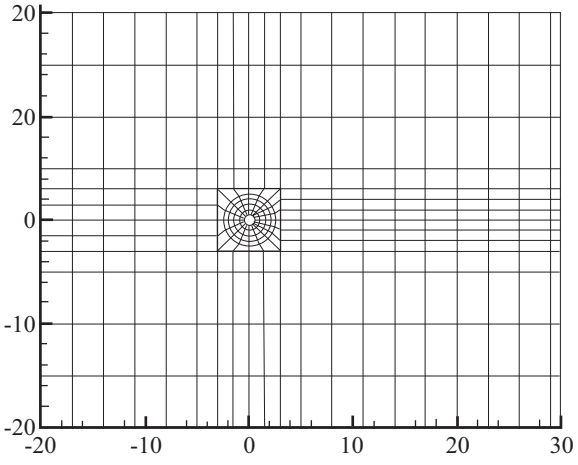


Fig. 2 Conforming mesh (K = 388, N = 11)

https://doi.org/10.1017/jmech.2016.77 Published online by Cambridge University Press

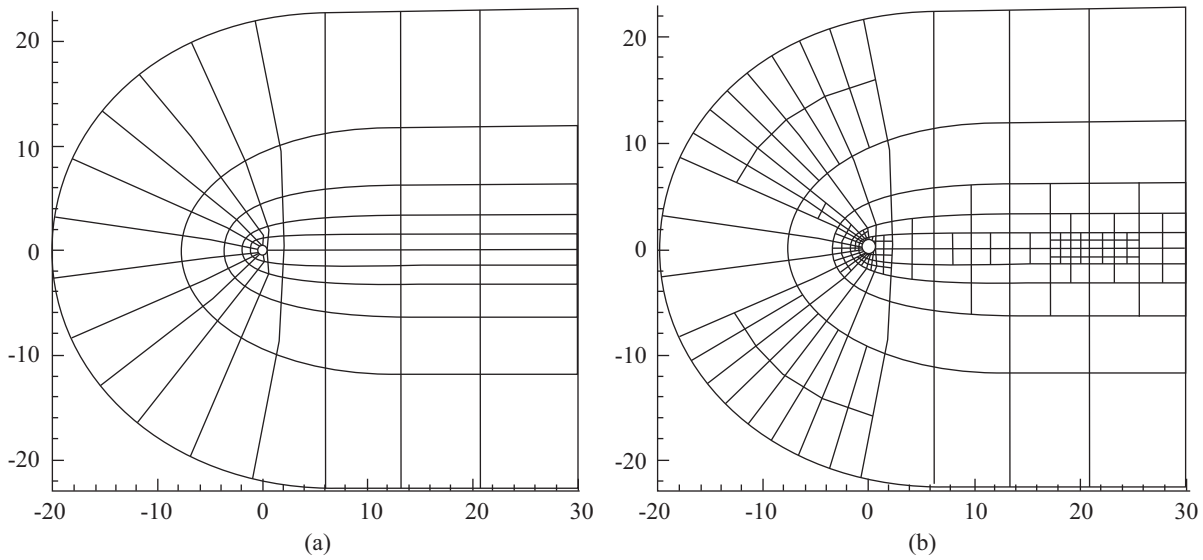


Fig. 3 (a) Initial mesh K = 95, (b) mesh refinement, started from t = 0, K = 95 to 249, N = 11, Re = 100.

the cylinder center, and a distance of 30D in downstream. The distance from upper and lower boundaries to cylinder center both are 20D. Uniform flow boundary conditions ($u = U_0$, $v = 0$) are employed in the inflow, upper and lower boundaries. The outflow boundary condition is employed in the most downstream boundary. The Reynolds numbers are varied from 40 to 250. For conforming approach, 388 macro spectral elements (K) are employed as shown in Fig. 2. The order (N) of basic shape function or Gauss-Lobatto-Legendre polynomial is 11.

4.2 Validation of Adaptive Nonconforming Scheme

The adaptive mesh scheme is tested in the case of flow past a circular cylinder in Re = 40 to look for the convergence and sufficient element number. The initial coarse grid, as shown in Fig. 3(a), has 95 elements with same domain dimension and boundary conditions as the conforming meshes as Fig. 2. The final element number are controlled in K = 103 to K = 297 after successive mesh refinements from the coarse mesh.

As increasing element number, the pressure coefficient along the surface of the cylinder by nonconforming meshes converge to the result of the case with 334 conforming elements as shown in Fig 4(a). Noticeably, the case of K = 103 with insufficient element number, the surface pressure coefficient is unstable.

The results of Fig. 4(a) show the nonconforming meshes with K = 182 holds the same accuracy with that of conforming meshes with K = 292, if the result of conforming meshes with element number, K = 334, order of N = 11 is regarded as the exact solution. Once the element number of nonconforming meshes is increased to the similar number as conforming one, the accuracy of nonconforming with K = 297 is better than that of conforming meshes with K = 292 as shown in Fig. 4(a). The corresponding mesh distributions are shown in Figs. 4(c) and (d). After comparing with other studies, the sufficient element number is 247 which values is between the numerical result of Park *et al*. [18] and experimental data of Thom intercepted from the report of Apelt [19] as shown in Fig. 4(b).

For Re > 49, such as Re = 140, the phenomenon of vortex shedding exists and the pressure coefficient along the surface of cylinder is no longer steady. To capture the resolution on cylinder surface and the vortex street in the wake area, more elements are deployed in these two areas by mesh refinement algorithm as shown in Fig. 3(b). The resolution required in wake is vorticity rather than pressure or velocity only. Therefore, the order of Legendre polynomial is increased to N = 11. A similar element number of conforming mesh with K = 244 is also tested to compare the accuracy with its counterpart, nonconforming mesh. The mean pressure coefficient is the average results of 10 vortex shedding cycles as shown in Fig. 4(e). The results indicate the mean pressure coefficients obtained by adaptive nonconforming method with 247 elements is much closer to that of Park *et al*. [18] than that of conforming mesh with K = 244. Once increasing element number in conforming mesh to K = 388, the result of conforming mesh is close to that nonconforming mesh and result of Park *et al*.

No matter in the steady case, Re = 40 or unsteady case, Re = 140, the accuracy of adaptive nonconforming meshes is better than that of conforming meshes. For reaching a specific accuracy, the element number required for adaptive nonconforming meshes is less than that of conforming meshes. This demonstrates the advantage and efficiency of present method.

4.3 Comparison of Nonconforming and Conforming Approaches

First, the results at Reynolds numbers, Re = 40 to 250, obtained by conforming spectral method are used as reference for comparison. For nonconforming approach, the initial coarse grid is employed as shown in Fig. 3(a) with 95 elements of shape function order 11. The initial meshes and its results were used as the inputs of the

https://doi.org/10.1017/jmech.2016.77 Published online by Cambridge University Press

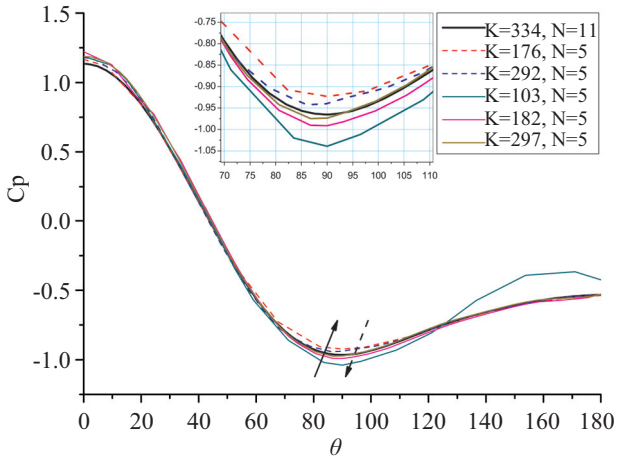


Fig. 4(a) Re = 40, convergence of the pressure coefficient along the surface of cylinder, obtained by adaptive nonconforming spectral element method by increasing total element numbers (K). Solid lines are obtained by nonconforming meshes; dashed lines are obtained by conforming meshes.

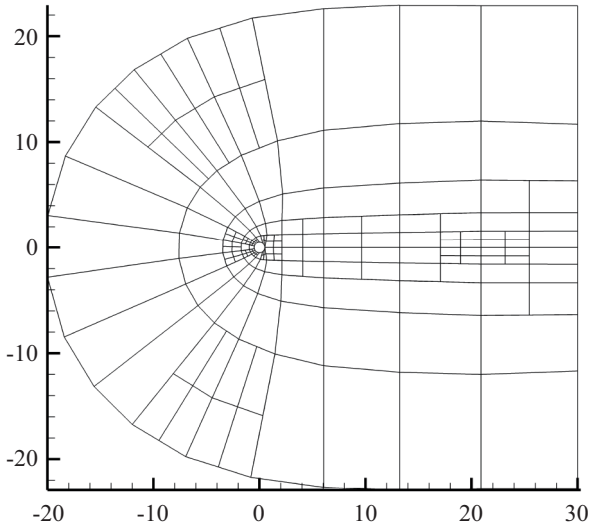


Fig. 4(b) nonconforming mesh with element number, K = 182.

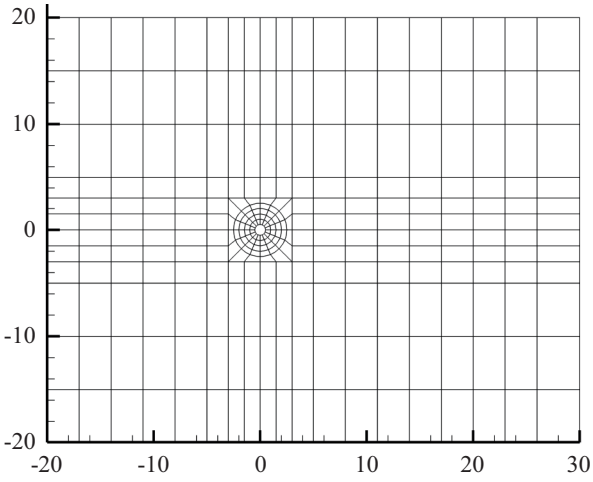


Fig. 4(c) conforming mesh with element number, K = 292.

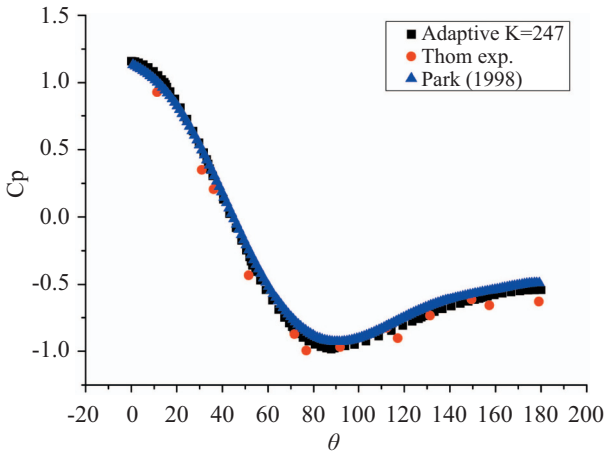


Fig. 4(d) Re = 40, comparison of pressure coefficients along the surface obtained from nonconforming spectral element method, other numerical and experimental results.

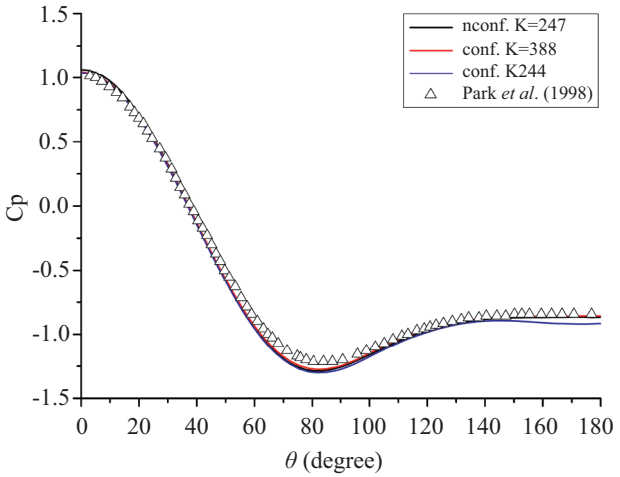


Fig. 4(e) Re = 140, comparison of pressure coefficients obtained from nonconforming and conforming methods.

mesh refinement process. After mesh refinement, the nonconforming meshes, as shown in Fig. 3(b), have 249 elements, which make up only 64% of conforming meshes (K = 388), as shown in Fig. 2. The vigorous mesh refinements take place in the windward side of cylinder and its wake region or the vortex street path where larger vorticity gradient exist. The advantages of the adaptive nonconforming meshes approach can be found by comparison with the conforming meshes approach with respect to streamline, vorticity contour, error reduction as well as computational efficiency. The vorticity of Re = 100 can be found in Fig. 5(a) for conforming and Fig. 5(b) for nonconforming meshes, respectively, where the vorticity distributions on the vortex street are identical to each other. A closer look at vorticity contours can be found in Fig. 6, where the vorticity contours of the adaptive nonconforming approach agree with conforming ones in good resolution. Several tiny meshes are employed around the cylinder after mesh refinement as shown in Fig. 6(b). In higher Reynolds number such as Re = 140 and 200,

https://doi.org/10.1017/jmech.2016.77 Published online by Cambridge University Press

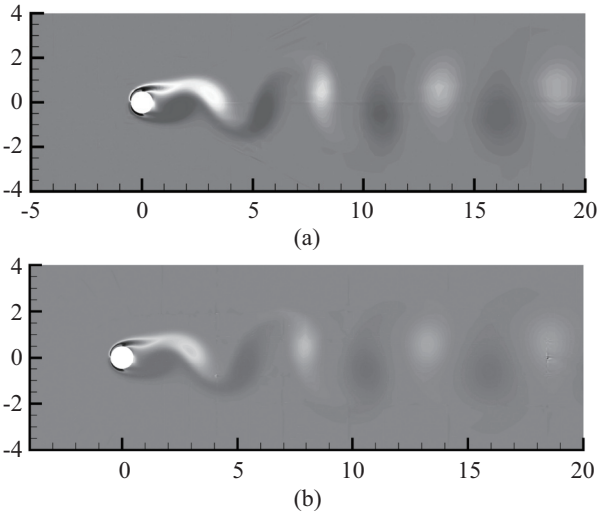


Fig. 5 Vorticity plots, Re = 100 (a)conforming method (b) adaptive nonconforming method.

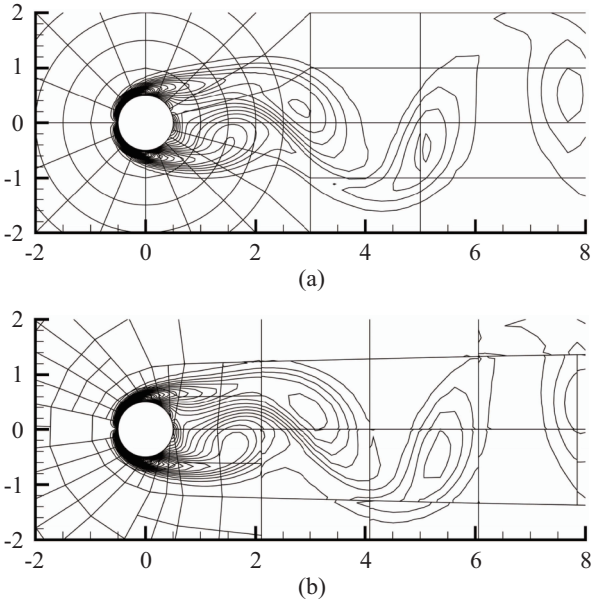


Fig. 6 Re = 100, a close look of vorticity contours, (a) conforming method, (b) adaptive nonconforming method

though the major adaptive mesh distribution is almost that same as that of Re = 100, there is more enhanced mesh distribution near the windward side of cylinder in Re = 140 and 200 than that in Re = 100 as seen when comparing Fig. 6(b) and Fig. 8(b).

For Re = 200, the results obtained by the adaptive nonconforming approach show the resolution as good as that obtained by the conforming approach as seen in Fig. 7. A closer comparison of vorticity contour can be found in Fig. 8 (a) and (b) where the resolution obtained by the adaptive meshes approach is better than that of the conforming method.

4.4 Quantitative Comparison

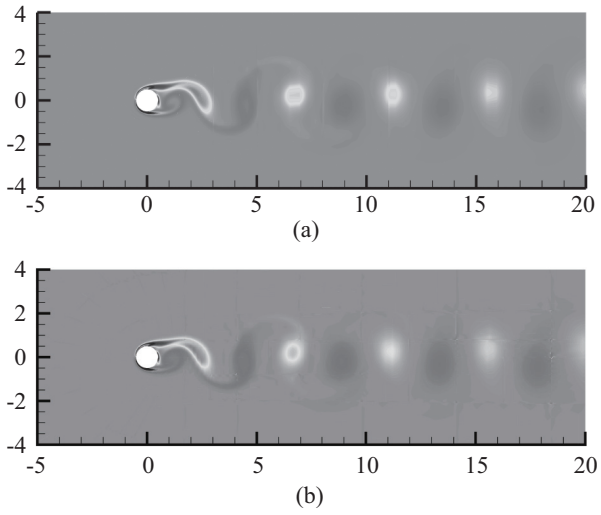


Fig. 7 Vorticity plots, Re = 200 (a)conforming method (b) adaptive nonconforming method.

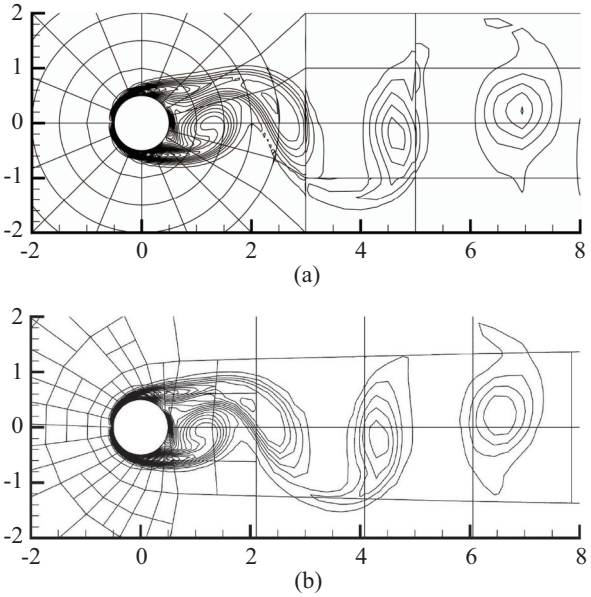


Fig. 8 Re = 200, a close look of vorticity contours, (a) conforming method (b) adaptive nonconforming method.

4.4.1 Strouhal Number

For the Strouhal number of vortex shedding as shown in Table 1, the results from the both adaptive nonconforming methods deviate less than 0.81% from the ones of the conforming method. Especially, the results of the vorticity error based adaptive nonconforming method (vorticity based nonconforming method) only deviates from those of the conforming method by 0.05~0.24%. As further comparison with other experimental results as well as numerical studies listed in Table 2, the Strouhal number of Re = 100 with the vorticity based nonconforming method deviates by 1.53% from the result of Posdziech and Grundmann [20], where the computational domain is 4000 times the diameter of the cylinder. However, the result of vorticity based nonconforming

https://doi.org/10.1017/jmech.2016.77 Published online by Cambridge University Press

Table 1 Drag, Life coefficient and Strouhal number comparison by different non-conforming approaches.

Methods		Conforming (K = 388)	Adaptive nonconforming (K = 249)		Posdziech [20] ($L_{b|i}$/D = 20)
			Vorticity (dev.[1], dev.[2])	V&P (dev.[1], dev.[2])	
St.	Re = 100	0.1662	0.1658 (0.24%, 0.5%)	0.1652 (0.60%, 0.89%)	0.1667
	Re = 200	0.1944	0.1943 (0.05%, 1.67%)	0.1960 (0.81%, 0.80%)	0.1976
Cd	Re = 100	1.3485	1.3466 (0.14%, 0.28%)	1.3407(0.57%, 0.7%)	1.3504
	Re = 200	1.3483	1.350(0.1%, 0.1%)	1.3440 (0.3%, 0.37%)	1.3490
Cl	Re = 100	0.3300	0.3299 (0.03%, 0.3%)	0.3276(0.7%, 0.99%)	0.3309
	Re = 200	0.6869	0.6872(0.04%, 0.1%)	0.6831(0.55%, 0.71%)	0.6880

Notes:
Conforming: Conforming mesh (k = 388)
Vorticity: Vorticity error based method (k = 249)
V&P: Synthesis of velocity and pressure error based method
dev[1]: The deviation between the results of the adaptive meshes method and those of the conforming meshes.
dev[2]: The deviation between the results of the adaptive meshes method and those from Posdziech [20]($L_{b|i}$/D = 20).
St: Strouhal number
Cd: Drag coefficient
Cl: Lift coefficient

Table 2 Strouhal number Comparison.

		Nonconforming method (vorticity error based)				Conforming method			
		Re = 100		Re = 200		Re = 100		Re = 200	
Num	Present	0.1658	Dev.%	0.1943	Dev.%	0.1662	Dev. %	0.1944	Dev.%
	Rajani [25]	0.1569	5.67	0.1957	0.71	0.1569	5.93	0.1957	0.66
	Posdziech 20D [20]	0.1667	0.5	0.1976	1.66	0.1667	0.2	0.1976	1.67
	Posdziech 4000D [20]	0.1633	1.53	0.1940	0.15	0.1633	1.78	0.1940	0.21
Exp	Williamson [22, 23]	0.1643	0.91	0.183	6.17	0.1643	1.14	0.183	6.23
	Hammanche [21]	0.1658	0	-	-	0.1658	0.24	-	-
	Roshko [26]	0.167	0.718	0.19	2.3	0.167	0.48	0.19	2.3
	Norberg [27]	0.164	1.097	0.181	7.34	0.164	1.34	0.181	7.4

Note:
Num: Numerical results
Exp: Experimental results
Dev.: Deviation
20D: The upstream, upper and lower boundaries of the computational domain to the center of the cylinder, $L_{b|i}$/D = 20
4000D: $L_{b|i}$/D=4000

method is much closer to experimental results, such as those of Hammanche [21] and Williamson [22], with deviation of less than 0.91%. For Re = 200, the result of vorticity based nonconforming method deviates from other numerical results by 0.15~0.71% only, but by 6.17% from the experimental result of Williamson *et al*. [22, 23] due to the limitations of two-dimensional computation.

In summary, the Strouhal numbers obtained by vorticity based nonconforming method with 64% of conforming meshes in different Reynolds number are not only almost identical to those from conforming method but also reach good agreement with most of experimental [22] and numerical results [24, 28], especially, the result of Posdziech [20], in which the upstream domain is extended to 70 and 4000 times the diameter of the cylinder as shown in Fig. 9 (a).

4.4.2 Surface Forces

The accuracy of the force exerted on the surface of the cylinder can be examined by looking at the drag and lift coefficients in the nonconforming and conforming methods, respectively. The lift coefficient history diagrams obtained from the vorticity based nonconforming method are identical to those of the conforming approach, as shown in Fig. 10(a) for Re = 100 and Fig.11(a) for Re = 200, respectively. In addition, basically, the drag coefficient computed from vorticity based nonconforming method preserves the same frequency and amplitude as those obtained by conforming method. Though, for Re = 100, there is minor difference in the mean drag coefficient between the conforming and the vorticity based nonconforming methods as shown in Fig. 10(b), for Re = 200, results from both methods are almost identical as seen in Fig. 11(b).

The upstream, upper and lower boundaries of the computational domain to the center of the cylinder, $L_{b|i,}$ affects the mean drag coefficient, profoundly, as the report by Posdsiech [20]. The mean drag coefficient in Re = 70 to 250 from the present computation are exactly the same as in the results of Henderson [24] which domain size is closest to that of present study as seen in Fig. 9(b). The mean drag coefficient of vorticity based nonconforming method deviate at most by about 3%

https://doi.org/10.1017/jmech.2016.77 Published online by Cambridge University Press

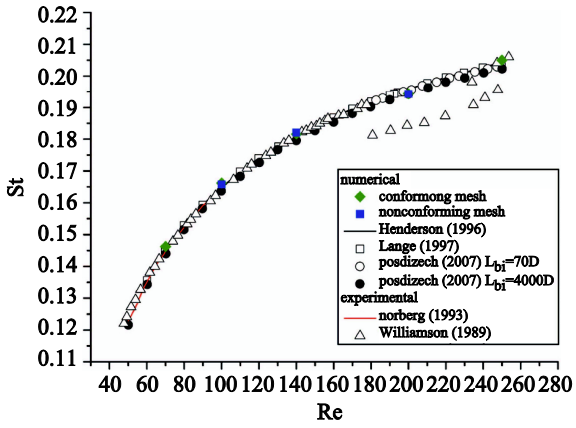


Fig. 9(a) Strouhal number in variant Reynolds numbers. The comparison of conforming and noncomforming results with data from Posdziech [20].

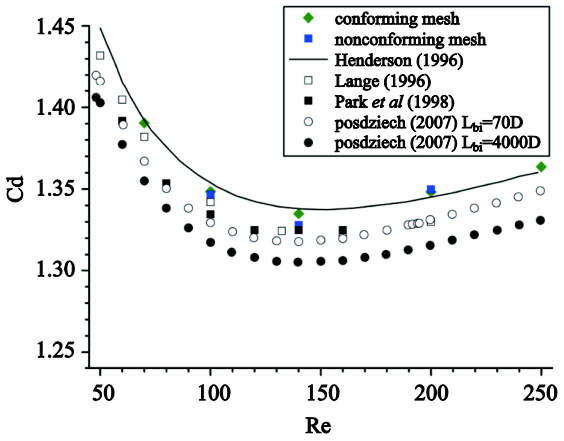


Fig. 9(b) Mean drag coefficient in variant Reynolds numbers. The comparison of conforming and nonconforming results with data from Posdziech [20].

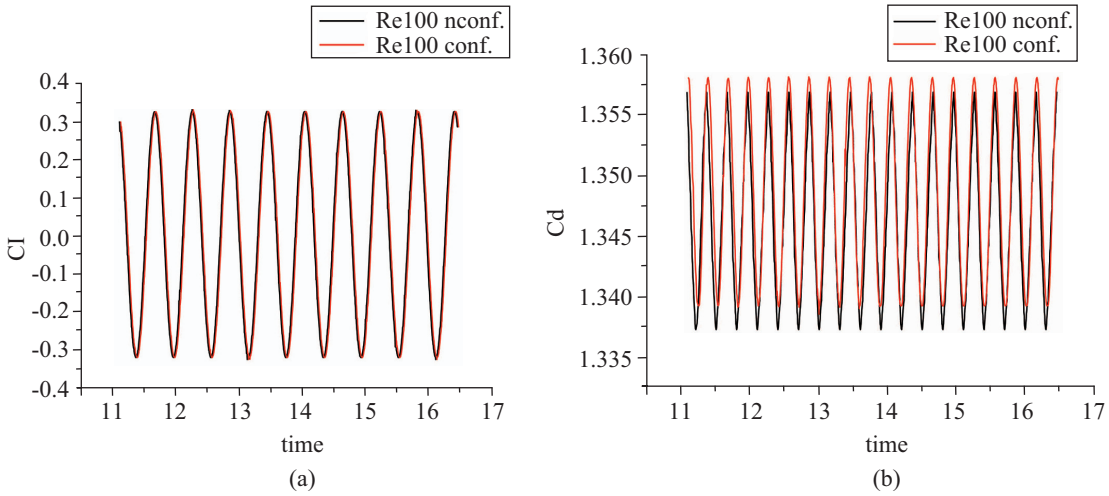


Fig. 10 Comparison with conforming and nonconforming approaches, Re = 100, (a) lift coefficient history (b) drag coefficient history.

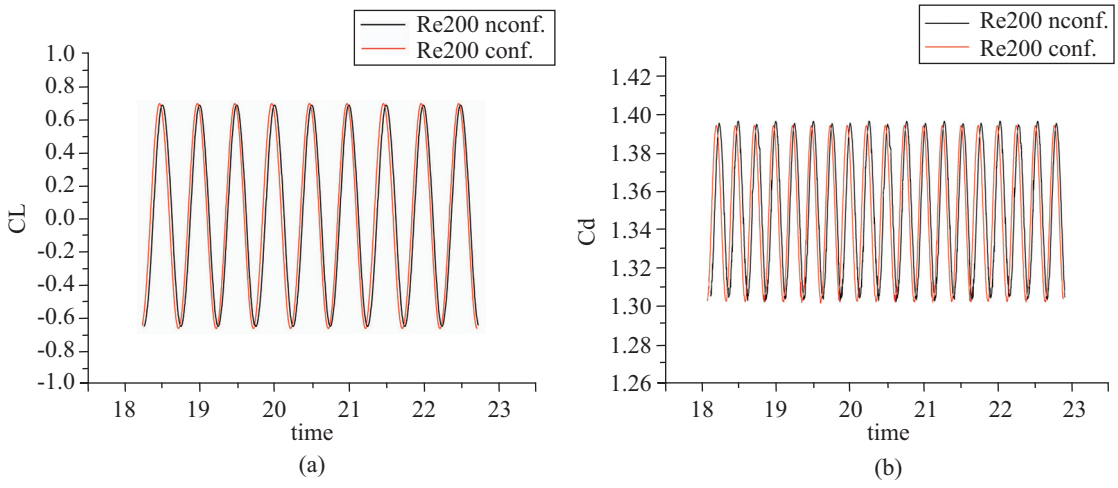


Fig. 11 Comparison with conforming and nonconforming approaches, Re = 200, (a) lift coefficient history (b) drag coefficient history.

https://doi.org/10.1017/jmech.2016.77 Published online by Cambridge University Press

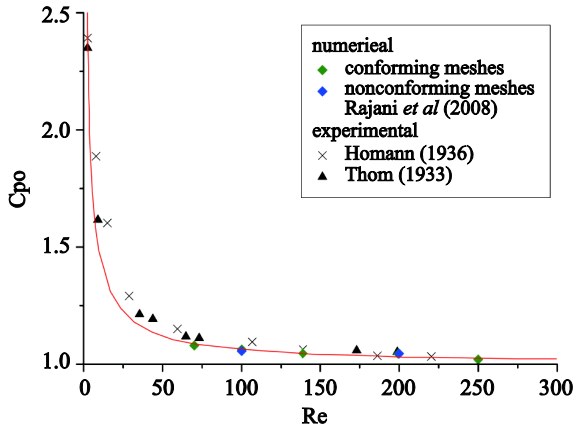


Fig. 12(a) Stagnation pressure coefficient comparison of conforming, nonconforming results and data from Rajani [25].

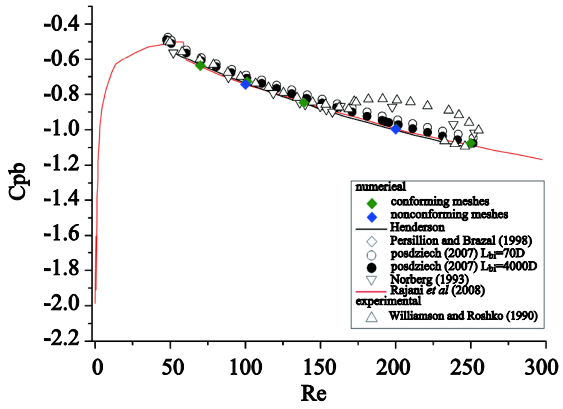


Fig. 12(b) Base pressure coefficient comparison of conforming, nonconforming results and data from Posdziech [20] and Rajani [25].

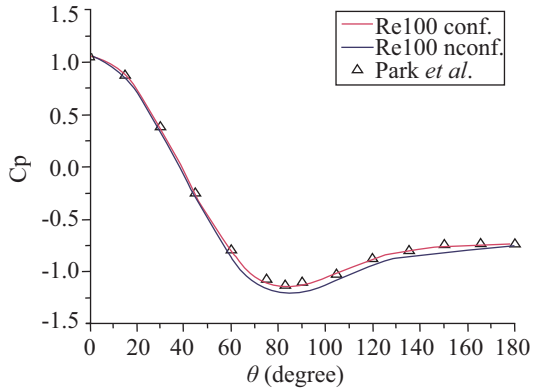


Fig. 13(a) Re = 100, cylinder surface pressure coefficient comparison of conforming method, noncomforming method and other numerical result

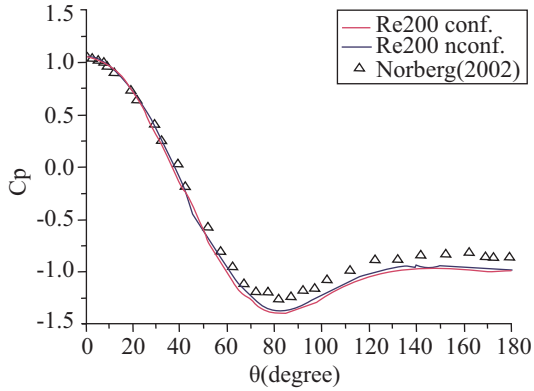


Fig. 13(b) Re = 200, cylinder surface pressure coefficient comparison of conforming method, noncomforming method and measurement

comparing with those of previous studies [20, 24, 28] where the longest front part of computational domain is extended to 4000 times diameter.

The mean values of these surface forces of the adaptive nonconforming mesh refinement based on two kinds of estimated error, namely, vorticity and synthesis of velocity and pressure, are listed in Table 1 for the sake of comparison. The mean drag coefficients from vorticity based nonconforming method deviated from those of conforming meshes by 0.14% for Re = 100 and 0.1% for Re = 200, respectively. The results of vorticity based nonconforming method also deviate slightly by 0.1~0.28% from the results found by Posdziech [20], in which upstream, upper and lower boundaries are the same as those obtained by present computation. The lift coefficient from the vorticity based nonconforming method is almost identical to that of conforming method with deviations of 0.03% for Re = 100 and 0.04% for Re = 200, respectively. The lift coefficients of vorticity based method also deviate slightly by 0.1~0.3% from those of Posdziech [20].

Though, the deviations from the results of the synthesis of velocity and pressure estimated error based nonconforming method (V&P method) are augmented slightly compared with those from of the vorticity based nonconforming method as shown Table 1, this nonconforming approach also provides satisfactory results with less than 0.99% deviation in surface forces.

The stagnation pressure coefficient, C_{po}, obtained by vorticity based nonconforming method makes good agreement with the conforming method and previous numerical [25] as well as experimental results [29, 30], as shown in Fig. 12(a). The base pressure coefficient, C_{pb}, of the vorticity based nonconforming method matches well with other numerical results [20, 24, 25, 31] as shown in Fig. 12(b). As Reynolds number is larger than 150, most of numerical results deviated from experimental one [23] because of the limitation of two-dimensional computation.

4.4.3 Local Property Comparison

In addition to the comparison in Strouhal number, drag and lift history, a local property such as the pressure coefficient along the cylindrical surface obtained from nonconforming approaches, vorticity based nonconforming method, is compared with those by conforming method

https://doi.org/10.1017/jmech.2016.77 Published online by Cambridge University Press

and other studies. From Fig. 13(a), the pressure coefficients of the nonconforming and conforming methods along the cylinder surface for Re = 100 are close to each other and the numerical result of Park *et al.* [18]. For Re = 200,the nonconforming and conforming methods have the same surface Cp values, which slightly differ from the experimental result of Norberg [32] behind the separation point due to the three-dimensional instability, as shown in Fig. 13(b).

4.5 Performance of Indicators

Besides the comparison of physical properties, an index is nenecessary to indicate the mesh refinement quality. The global L^2 error is the square root of the sum of each elemental estimated error square which is composed of truncation and quadrature errors as shown in Eq. (24).

$$\varepsilon_{est}^{global} = \left(\sum_{k=1}^{K} \left(\frac{(a_N^k)^2}{\frac{2N+1}{2}} + \int_{N+1}^{\infty} \frac{(a_n^k(n))^2}{\frac{2n+1}{2}} dn \right) \right)^{\frac{1}{2}} \tag{24}$$

The global estimated L^2 error ranges the whole computational domain rather than just an individual element. Hence, this index can represent global accuracy, error decay rate and computational efficiency. Three kinds of properties, the synthesis of velocity and pressure estimated error, vorticity estimated error and estimated error decay rate (σ) are used as the indicators of mesh refinement and their corresponding global L^2 error are recorded to compare their efficiencies.

For Re = 100, within the same physical time in simulation, e.g. t = 0.4, the CPU time spent by the nonconforming approach is much less than that of the conforming method, as shown in Fig. 14(a). Among those, the time spent by vorticity based nonconforming method is only 20% of that of conforming method. As seen in Fig. 14(b), the estimated global L^2 errors of all nonconforming mesh methods are reduced sharply as the physical time goes on with increasing element number, though the initial errors are larger due to the initial coarse meshes. However, as time goes on, the errors of nonconforming approaches are reduced to be lower than that of conforming method because the meshes are refined

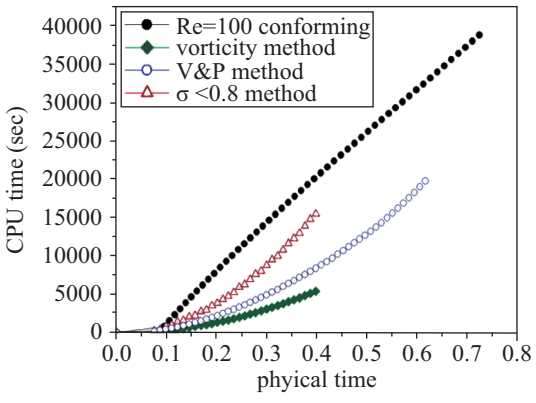


Fig. 14(a)CPU time lapse in instant simulated physical time scale, Re = 100.

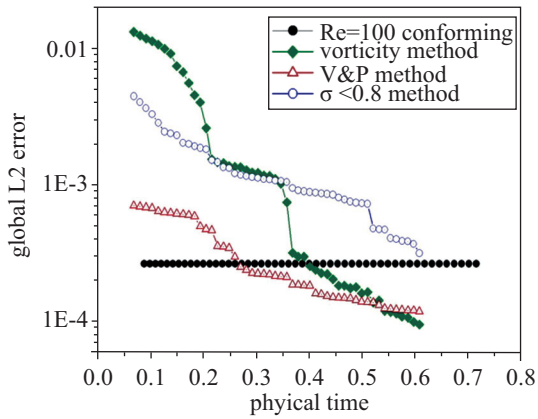


Fig. 14(b) Global error decay time rate in simulated physical time scale, Re = 100.

in the proper regions such as indicated by vorticity based nonconforming and V&P methods. Hence, under same physical time, the nonconforming approach not only takes much less CPU time than that of conforming approach but its error reduction rate is faster than that of conforming method, as long as the appropriate mesh refinement indicator is selected.

This conclusion also can be applied in the case of Re = 200, as shown in Figs. 15(a) and (b) where vorticity based nonconforming method gives better accuracy and efficiency than all other methods.

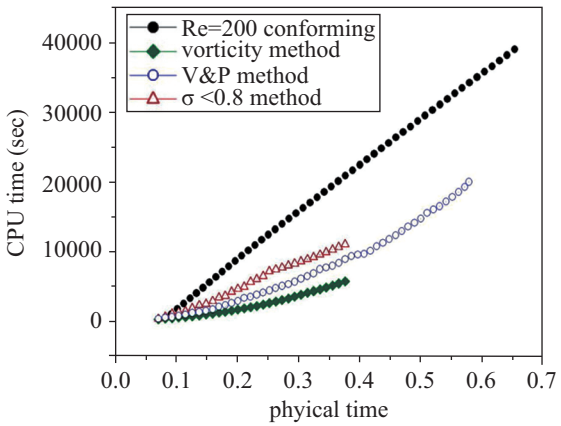


Fig. 15(a) CPU time lapse in instant simulated physical time scale, Re = 200.

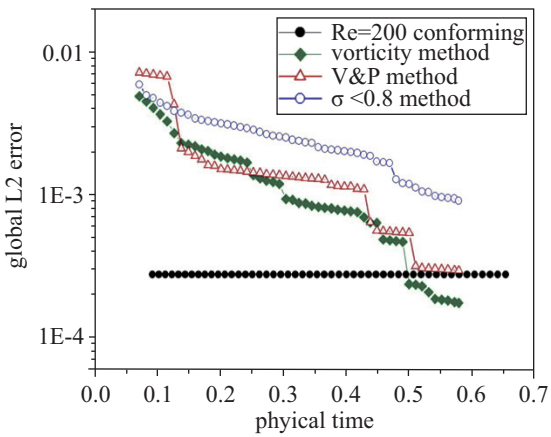


Fig. 15(b) Global error decay time rate in simulated physical time scale, Re = 200.

https://doi.org/10.1017/jmech.2016.77 Published online by Cambridge University Press

5. CONCLUSIONS

The adaptive nonconforming spectral element method has been demonstrated its feasibility on curved elements. Three kinds of properties, including the estimated error of synthesis of velocity and pressure, vorticity estimated error and estimated error decay rate (σ), are used as mesh refinement indicators for the adaptive nonconforming methods. Among those, the vorticity error based method provide best accuracy which is similar to the conforming method and other numerical and experimental results with less computational cost. This study shows the vorticity error based adaptive nonconforming spectral element method is an efficient and practical technique and applicable on the simulations of flow past objects with more general geometry such as tube bank to study its vortex dynamics and heat transfer problems further.

ACKNOWLEDGEMENTS

The authors are grateful to National Yunlin University of Science and Technology for the financial support, under the grant No.105H500214.

REFERENCES

1. Patera, A. T., "A spectral element method for fluid dynamics: laminar flow in a channel expansion," *Journal of Computational Physics*, **54**, pp. 468-488 (1984).
2. Maday, Y., Mavriplis, C. and Patera, A.T., "Nonconforming mortar element methods: Application to spectral discretization," *Domain Decomposition Methods,* Chan, T., Periaux, J., Widlund, O.B., Eds., SIAM, Philadelphia, pp. 392-418 (1989).
3. Bernardi, C., Maday, Y. and Patera, A.T., "A new nonconforming approach to domain decomposition: the mortar element method," *Non-linear Partial Differential Equations and their Applications*, Brezis, H., Lions, J. L., Eds., Pitman/Wiley: Lon-don/New York, **11**, pp.13-51 (1994).
4. Mavriplis, C. and Hsu, L.-C., "A two-dimensional adaptive spectral element method," *Proceedings of the 13th AIAA Computational Fluid Dynamics Conference, Snowmass*, USA (1997).
5. Feng, H. and Mavriplis, C., "Adaptive spectral element simulations of thin premixed flame sheet deformations," *Journal of Scientific Computing*, **17**, pp. 385-395 (2002).
6. Feng, H. and Mavriplis , C., Van der Wijngaart, R. and Biswas, R., "Parallel 3D mortar element method for adaptive nonconforming meshes," *Journal of Scientific Computing*, **27**, pp. 231-243 (2006).
7. Henderson, R. D. "Dynamic refinement algorithms for spectral element methods," *Computer Methods in Applied Mechanics and Engineering*, **175**, pp. 395-411 (1999).
8. Premasuthan, S., Liang, C. and Jameson, A. "Computation of flows with shocks using the Spectral Difference method with artificial viscosity, II: Modified formulation with local mesh refinement," *Computers & Fluids*, **98**, pp. 122-133 (2014).
9. Kopera, M. A. and Giraldo, F. X. "Analysis of adaptive mesh refinement for IMEX discontinuous Galerkin solutions of the compressible Euler equations with application to atmospheric simulations," *Journal of Computational Physics*, **275**, pp. 92-117 (2014).
10. Dupont, F. and Lin, C. "The adaptive spectral element method and comparisons with more traditional formulations for ocean modeling," *Journal of Atmosphere and Ocean Technology*, **21**, pp. 135-147 (2004).
11. Orszag, S.A. and Kells, L.C. "Transition to turbulence in plane poiseuille and plane couette flow," *Journal of Fluid Mechanics*, **96**, pp. 159-205 (1980).
12. Gear, C. W., *Numerical Initial Value Problems in Ordinary Differential Equations*, Prentice-Hall, Englewood Cliffs, New Jersey, (1971).
13. Golub, G. H. and Van Loan, C. F., *Matrix Computations*, The Johns Hopkins University Press, Baltimore, (1985).
14. Mavriplis, C. "Nonconforming Discretizations and a Posteriori Error Estimators for Adaptive Spectral Element Techniques", Ph. D. Dissertation, Department of Aeronautics and Astronautics, Massachusetts Institute of Technology, Massachusetts, U.S. (1989).
15. Oh, W.S., Kim, J.S. and Kwon, O.J. "Time-accurate Navier–Stokes simulation of vortex convection using an unstructured dynamic mesh procedure," *Computers & Fluids*, **32**, pp. 727-749 (2003).
16. Rausch, R.D., Batina, J.T. and Yang, H.T.Y., "Spatial adaptation of unstructured meshes for unsteady aerodynamic flow computations," *AIAA Journal*, **30**, pp. 1243-1251 (1992).
17. Hwang, C. J. and Kuo, J. Y. "Adaptive finite volume upwind approaches for aeroacoustic computations," *AIAA Journal*, **35**, pp. 1286-1293 (1997).
18. Park, J., Kwon, K. and Choi, H., "Numerical solutions of flow past a circular cylinder at Reynolds numbers up to 160," *KSME International Journal*, **12**, pp. 1200-1205 (1998).
19. Apelt, C. "The Steady flow of viscous fluid past a circular cylinder at Reynolds number 40 to 44," *A.R.C. Technical Report, R & M. No. 3175*, Aeronautical Research Council, Ministry Of Aviation, London (1961).
20. Posdziech, O. and Grundmann, R. "A systematic approach to the numerical calculation of fundamental quantities of the two-dimensional flow over a circular cylinder," *Journal of Fluids and Structures*, **23**, pp. 479-499 (2007).
21. Hammache, M. and Gharib M. "An experimental

https://doi.org/10.1017/jmech.2016.77 Published online by Cambridge University Press

study of the parallel and oblique vortex shedding from circular cylinders," *Journal of Fluid Mechanics*, **232**, pp. 567-590 (1991).

22. Williamson, C. H. K., "The existence of two stages in the transition to three dimensionality of a cylinder wake," *Physics of Fluids*, **31**, pp. 3165-3168 (1988).
23. Williamson, C. H. K. and Roshko, A., "Measurements of base pressure in the wake of a cylinder at low Reynolds numbers," *Zeitschrift Flugwissenschaften und Weltraumforschung*, **14**, pp. 38-46 (1990).
24. Henderson, R. D., "Details of the drag curve near the onset of vortex shedding," *Physics of Fluids*, **7**, pp. 2102-2104 (1995).
25. Rajani, B.N., Kandasamy, A. and Majumdar, S., "Numerical simulation of laminar flow past a circular cylinder," *Applied Mathematical Modeling*, **33**, pp. 1228-1247 (2009).
26. Roshko A., "On the development of turbulent wakes from vortex streets," *NACA Report 1191* (1954).
27. Norberg, C., "An experimental investigation of the flow around a circular cylinder: influence of aspect ratio," *Journal of Fluid Mechanics*, **258**, pp. 287-316 (1994).
28. Lange, C., "Numerical predictions of heat and momentum transfer from a cylinder in crossflow with implications to hot-wire anemometry". Ph.D. Dissertation, Friedrich-Alexander University Erlangen-Nürnberg, Germany (1997).
29. Homann, F., "Influence of higher viscosity on flow around cylinder," *Forsch. Gebiete Ingenieur*, **17**, pp. 1-10 (1936).
30. Thom, A., "The flow past circular cylinder at low speeds," *Proeedingc Royal Society Series A*, **141**, pp. 651-669 (1933).
31. Persillon, A. and Braza, M., "Physical analysis of the transition to turbulence in the wake of a circular cylinder by three-dimensional Navier–Stokes simulation," *Journal of Fluid Mechanics*, **365**, pp. 23-88 (1998).
32. Norberg, C., "Pressure distributions around a circular cylinder in cross-flow," *Symposium on Bluff Body Wakes and Vortex-Induced Vibrations (BBVIV3)*, Hourigan, K., Leweke, T., Thompson, M.C., Williamson, C.H.K. Eds., Port Arthur, Queensland, Australia, Monash University, Melbourne, Australia, pp. 1-4 (2002).

(Manuscript received March 1, 2016,
accepted for publication May 16, 2016.)

https://doi.org/10.1017/jmech.2016.77 Published online by Cambridge University Press